

# 3DShape2VecSet: A 3D Shape Representation for Neural Fields and Generative Diffusion Models

BIAO ZHANG, KAUST, Saudi Arabia  
 JIAPENG TANG, TU Munich, Germany  
 MATTHIAS NIESSNER, TU Munich, Germany  
 PETER WONKA, KAUST, Saudi Arabia

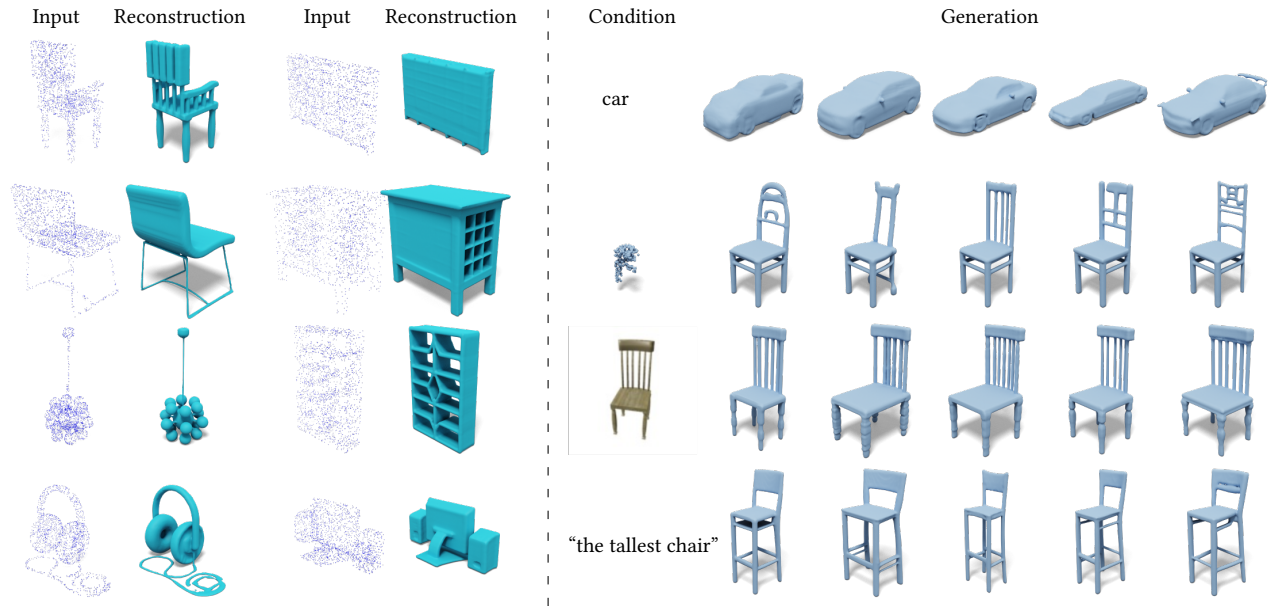


Fig. 1. **Left:** Shape autoencoding results (surface reconstruction from point clouds) **Right:** the various down-stream applications of **3DShape2VecSet** (from top to bottom): (a) category-conditioned generation; (b) point clouds conditioned generation (shape completion from partial point clouds); (c) image conditioned generation (shape reconstruction from single-view images); (d) text-conditioned generation.

We introduce 3DShape2VecSet, a novel shape representation for neural fields designed for generative diffusion models. Our shape representation can encode 3D shapes given as surface models or point clouds, and represents them as neural fields. The concept of neural fields has previously been combined with a global latent vector, a regular grid of latent vectors, or an irregular grid of latent vectors. Our new representation encodes neural fields on top of a set of vectors. We draw from multiple concepts, such as the radial basis function representation and the cross attention and self-attention function, to design a learnable representation that is especially suitable for processing with transformers. Our results show improved performance in 3D shape encoding and 3D shape generative modeling tasks. We demonstrate a wide variety of generative applications: unconditioned generation, category-conditioned generation, text-conditioned generation, point-cloud completion, and image-conditioned generation. Code: <https://1zb.github.io/3DShape2VecSet/>.

Additional Key Words and Phrases: 3D Shape Generation, 3D Shape Representation, Diffusion Models, Shape Reconstruction, Generative models

Authors' addresses: Biao Zhang, KAUST, Saudi Arabia, biao.zhang@kaust.edu.sa; Jiapeng Tang, TU Munich, Germany, jiapeng.tang@tum.de; Matthias Nießner, TU Munich, Germany, niessner@tum.de; Peter Wonka, KAUST, Saudi Arabia, peter.wonka@kaust.edu.sa.

## 1 INTRODUCTION

The ability to generate realistic and diverse 3D content has many potential applications, including computer graphics, gaming, and virtual reality. To this end, many generative models have been explored, *e.g.*, generative adversarial networks, variational autoencoders, normalizing flows, and autoregressive models. Recently, diffusion models have emerged as one of the most popular method with fantastic results in the 2D image domain [Ho et al. 2020; Rombach et al. 2022] and have shown their superiority over other generative methods. For instance, it is possible to do unconditional generation [Karras et al. 2022; Rombach et al. 2022], text conditioned generation [Rombach et al. 2022; Saharia et al. 2022], and generative image inpainting [Lugmayr et al. 2022]. However, the success in the 2D domain has not yet been matched in the 3D domain.

In this work, we will study diffusion models for 3D shape generation. One major challenge in adapting 2D diffusion models to 3D is the design of a suitable shape representation. The design of such a shape representation is the major focus of our work, and we will discuss several design choices that lead to the development of our proposed representation.

Different from 2D images, there are several predominant ways to represent 3D data, *e.g.*, voxels, point clouds, meshes, and neural fields. In general, we believe that surface-based representations are more suitable for downstream applications than point clouds. Among the available choices, we choose to build on neural fields as they have many advantages: they are continuous, represent complete surfaces and not only point samples, and they enable many interesting combinations of traditional data structure design and representation learning using neural networks.

Two major approaches for 2D diffusion models are to either use a compressed latent space, *e.g.*, latent diffusion [Rombach et al. 2022], or to use a sequence of diffusion models of increasing resolution, *e.g.*, [Ramesh 2022; Saharia et al. 2022]. While both of these approaches seem viable in 3D, our initial experiments indicated that it is much easier to work with a compressed latent space. We therefore follow the latent diffusion approach.

A subsequent design choice for a latent diffusion approach is to decide between a learned representation or a manually designed representation. A manually designed representation such as wavelets [Hui et al. 2022] is easier to design and more lightweight, but in many contexts learned representations have shown to outperform manually designed ones. We therefore opt to explore learned representations. This requires a two-stage training strategy. The first stage is an autoencoder (variational autoencoder) to encode 3D shapes into a latent space. The second stage is training a diffusion model in the learned latent space.

In the case of training diffusion models for 3D neural fields, it is even more necessary to generate in latent space. First, diffusion models often work with data of fixed size (*e.g.*, images of a given fixed resolution). Second, a neural field is a continuous real-valued function that can be seen as an infinite-dimensional vector. For both reasons, we decide to find a way to encode shapes into latent space before all else (as well as a decoding method for reverting latents back to shapes).

Finally, we have to design a suitable learned neural field representation that provides a good trade-off between compression and reconstruction quality. Such a design typically requires three components: a spatial data structure to store the latent information, a spatial interpolation method, and a neural network architecture. There are multiple options proposed in the literature shown in Fig. 2. Early methods used a single global latent vector in combination with an MLP network [Mescheder et al. 2019; Park et al. 2019]. This concept is simple and fast but generally struggles to reconstruct high-quality shapes. Better shape details can be achieved by using a 3D regular grid of latents [Peng et al. 2020] together with tri-linear interpolation and an MLP. However, such a representation is too large for generative models and it is only possible to use grids of very low resolution (*e.g.*,  $8 \times 8 \times 8$ ). By introducing sparsity, *e.g.*, [Yan et al. 2022; Zhang et al. 2022], latents are arranged in an irregular grid. The latent size is largely reduced, but there is still a lot of room for improvement which we capitalize on in the design of 3DShape2VecSet.

The design of 3DShape2VecSet combines ideas from neural fields, radial basis functions, and the network architecture of attention layers. Similar to radial basis function representation for continuous functions, we can also re-write existing methods in a similar form

(linear combination). Inspired by cross attention in the transformer network [Vaswani et al. 2017], we derived the proposed latent representation which is a fixed-size set of latent vectors. There are two main reasons that we believe contribute to the success of the representations. First, the representation is well-suited for the use with transformer-based networks. As transformer-based networks tend to outperform current alternatives, we can better benefit from this network architecture. Instead of only using MLPs to process latent information, we use a linear layer and cross-attention. Second, the representation no longer uses explicitly designed positional features, but only gives the network the option to encode positional information in any form it considers suitable. This is in line with our design principle of favoring learned representations over manually designed ones. See Fig. 2 e) for the proposed latent representation.

Using our novel shape representation, we can train diffusion models in the learned 3D shape latent space. Our results demonstrate an improved shape encoding quality and generation quality compared to the current state of the art. While pioneering work in 3D shape generation using diffusion models already showed unconditional 3D shape generation, we show multiple novel applications of 3D diffusion models: category-conditioned generation, text-conditioned shape generation, shape reconstruction from single-view image, and shape reconstruction from partial point clouds.

To sum up, our contributions are as follows:

- (1) We propose a new representation for 3D shapes. Any shape can be represented by a fixed-length array of latents and processed with cross-attention and linear layers to yield a neural field.
- (2) We propose a new network architecture to process shapes in the proposed representation, including a building block to aggregate information from a large point cloud using cross-attention.
- (3) We improve the state of the art in 3D shape autoencoding to yield a high fidelity reconstruction including local details.
- (4) We propose a latent set diffusion framework that improves the state of the art in 3D shape generation as measured by FID, KID, FPD, and KPD.
- (5) We show 3D shape diffusion for category-conditioned generation, text-conditioned generation, point-cloud completion, and image-conditioned generation.

## 2 RELATED WORK

In this section, we briefly review the literature of 3D shape learning with various data representations and 3D shape generative models.

### 2.1 3D Shape Representations

We mainly discuss the following representations for 3D shapes, including voxels, point clouds, and neural fields.

*Voxels.* Voxel grids, extended from 2D pixel grids, simply represent a 3D shape as a discrete volumetric grid. Due to their regular structure, early works take advantage of 3D transposed convolution operators for shape prediction [Brock et al. 2016; Choy et al. 2016; Dai et al. 2017; Girdhar et al. 2016; Wu et al. 2016, 2015]. A drawback of the voxels-based decoders is that the computational and memory costs of neural networks cubically increases with respect to

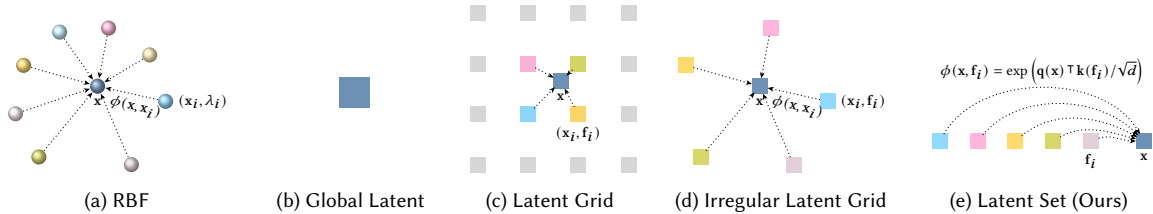


Fig. 2. **Continuous function representations.** Scalars are represented with spheres while vectors are cubes. The arrows show how spatial interpolation is computed.  $x_i$  and  $x$  are the coordinates of an anchor and a querying point respectively.  $\lambda_i$  is the SDF value of the anchor point  $x_i$  in (a).  $f_i$  is the associate feature vector located in  $x_i$  in (c)(d). The queried SDF/feature of  $x$  is based on the distance function  $\phi(x, x_i)$  in (a)(c)(d), while our proposed latent set representation (e) utilizes the similarity  $\phi(x, f_i)$  between querying coordinate and anchored features via a cross attention mechanism.

Table 1. **Neural fields for 3D shapes.** We categorize methods according to the position of the latents.

| # Latents | Latent Position | Methods                          |
|-----------|-----------------|----------------------------------|
| Single    | Global          | OccNet [Mescheder et al. 2019]   |
|           |                 | DeepSDF [Park et al. 2019]       |
|           |                 | IM-Net [Chen and Zhang 2019]     |
| Multiple  | Regular Grid    | ConvOccNet [Peng et al. 2020]    |
|           |                 | IF-Net [Chibane et al. 2020]     |
|           |                 | LIG [Jiang et al. 2020]          |
|           |                 | DeepLS [Chabra et al. 2020]      |
|           |                 | SA-ConvOccNet [Tang et al. 2021] |
|           |                 | NKF [Williams et al. 2022]       |
| Multiple  | Irregular Grid  | LDIF [Genova et al. 2020]        |
|           |                 | Point2Surf [Erler et al. 2020]   |
|           |                 | DCC-DIF [Li et al. 2022]         |
|           |                 | 3DILG [Zhang et al. 2022]        |
|           |                 | POCO [Boulch and Marlet 2022]    |
| Multiple  | Global          | Ours                             |

the grid resolution. Thus, most voxel-based methods are limited to low-resolution. Octree-based decoders [Häne et al. 2017; Meagher 1980; Riegler et al. 2017b,a; Tatarchenko et al. 2017; Wang et al. 2017, 2018] and sparse hash-based decoders [Dai et al. 2020] take 3D space sparsity into account, alleviating the efficiency issues and supporting high-resolution outputs.

*Point Clouds.* Early works on neural-network-based point cloud processing include PointNet [Qi et al. 2017a,b] and DGCNN [Wang et al. 2019]. These works are built upon per-point fully connected layers. More recently, transformers [Vaswani et al. 2017] were proposed for point cloud processing, e.g., [Guo et al. 2021; Zhang et al. 2022; Zhao et al. 2021]. These works are inspired by Vision Transformers (ViT) [Dosovitskiy et al. 2021] in the image domain. Points are firstly grouped into patches to form tokens and then fed into a transformer with self-attention. In this work, we also introduce a network for processing point clouds. Improving upon previous works, we compress a given point cloud to a small representation that is more suitable for generative modeling.

*Neural Fields.* A recent trend is to use neural fields as a 3d data representation. The key building block is a neural network which accepts a 3D coordinate as input, and outputs a scalar [Chen and

Table 2. **Generative models for 3d shapes.**

|                                       | Generative Models | 3D Representation |
|---------------------------------------|-------------------|-------------------|
| 3D-GAN [Wu et al. 2016]               | GAN               | Voxels            |
| I-GAN [Achlioptas et al. 2018]        | GAN*              | Point Clouds      |
| IM-GAN [Chen and Zhang 2019]          | GAN*              | Fields            |
| PointFlow [Yang et al. 2019]          | NF                | Point Clouds      |
| GenVoxelNet [Xie et al. 2020]         | EBM               | Voxels            |
| PointGrow [Sun et al. 2020]           | AR                | Point Clouds      |
| PolyGen [Nash et al. 2020]            | AR                | Meshes            |
| GenPointNet [Xie et al. 2021]         | EBM               | Point Clouds      |
| 3DShapeGen [Ibing et al. 2021]        | GAN*              | Fields            |
| DPM [Luo and Hu 2021]                 | DM                | Point Clouds      |
| PVD [Zhou et al. 2021]                | DM                | Point Clouds      |
| AutoSDF[Mittal et al. 2022]           | AR*               | Voxels            |
| CanMap [Cheng et al. 2022]            | AR*               | Point Clouds      |
| ShapeFormer[Yan et al. 2022]          | AR*               | Fields            |
| 3DILG [Zhang et al. 2022]             | AR*               | Fields            |
| LION [Zeng et al. 2022]               | DM*               | Point Clouds      |
| SDF-StyleGAN [Zheng et al. 2022]      | GAN               | Fields            |
| NeuralWavelet [Hui et al. 2022]       | DM*               | Fields            |
| TriplaneDiffusion [Shue et al. 2022]◊ | DM*               | Fields            |
| DiffusionSDF [Chou et al. 2022]◊      | DM*               | Fields            |
| Ours                                  | DM*               | Fields            |

\* Generative models in latent space.

◊ Works in submission.

Zhang 2019; Mescheder et al. 2019; Michalkiewicz et al. 2019; Park et al. 2019] or a vector [Chan et al. 2022; Mildenhall et al. 2020]. A 3D object is then implicitly defined by this neural network. Neural fields have gained lots of popularity as they can generate objects with arbitrary topologies and infinite resolution. The methods are also called *neural implicit representations* or *coordinate-based networks*. For neural fields for 3d shape modeling, we can categorize methods into global methods and local methods. 1) The global methods encode a shape with a single global latent vector [Mescheder et al. 2019; Park et al. 2019]. Usually the capacity of these kind of

methods is limited and they are unable to encode shape details. 2) The local methods use localized latent vectors which are defined for 3D positions defined on either a regular [Chibane et al. 2020; Jiang et al. 2020; Peng et al. 2020; Tang et al. 2021] or irregular grid [Boulch and Marlet 2022; Genova et al. 2020; Li et al. 2022; Zhang et al. 2022]. In contrast, we propose a latent representation where latent vectors do not have associated 3D positions. Instead, we learn to represent a shape as a list of latent vectors. See Tab. 1.

## 2.2 Generative models.

We have seen great success in different 2D image generative models in the past decade. Popular deep generative methods include generative adversarial networks (GANs) [Goodfellow et al. 2014], variational autoencoders (VAEs) [Kingma and Welling 2014], normalizing flows (NFs) [Rezende and Mohamed 2015], energy-based models [LeCun et al. 2006; Xie et al. 2016], autoregressive models (ARs) [Esser et al. 2021; Van Den Oord et al. 2017] and more recently, diffusion models (DMs) [Ho et al. 2020] which are the chosen generative model in our work.

In 3D domain, GANs have been popular for 3D generation [Achliopas et al. 2018; Chen and Zhang 2019; Ibing et al. 2021; Wu et al. 2016; Zheng et al. 2022], while only a few works are using NFs [Yang et al. 2019] and VAEs [Mo et al. 2019]. A lot of recent work employs ARs [Cheng et al. 2022; Mittal et al. 2022; Nash et al. 2020; Sun et al. 2020; Yan et al. 2022; Zhang et al. 2022]. DMs for 3D shapes are relatively unexplored compared to other generative methods.

There are several DMs dealing with point cloud data [Luo and Hu 2021; Zeng et al. 2022; Zhou et al. 2021]. Due to the high freedom degree of regressed coordinates, it is always difficult to obtain clean manifold surfaces via post-processing. As mentioned before, we believe that neural fields are generally more suitable than point clouds for 3D shape generation. The area of combining DMs and neural fields is still underexplored.

DreamFusion [Poole et al. 2022] explores how to extract 3D information from a pretrained 2D image diffusion model. The recent NeuralWavelet [Hui et al. 2022] first encodes shapes (represented as signed distance fields) into the frequency domain with the wavelet transform, and then train DMs on the frequency coefficients. While this formulation is elegant, generative models generally work better on learned representations. Some concurrent works [Chou et al. 2022; Shue et al. 2022] in submission also utilize DMs in a latent space for neural field generation. The TriplaneDiffusion [Shue et al. 2022] trains an autoencoder first for each shape. DiffusionSDF [Chou et al. 2022] runs a shape autoencoder based on triplane features [Peng et al. 2020].

*Summary of 3D generation methods.* We list several 3d generation methods in Tab. 2, highlighting the choice of generative model (GAN, DM, EBM, NF, or AR) and the choice of data structure to represent 3D shapes (point clouds, meshes, voxels or fields).

## 3 PRELIMINARIES

An attention layer [Vaswani et al. 2017] has three types of inputs: queries, keys, and values. Queries  $\mathbf{Q} = [\mathbf{q}_1, \mathbf{q}_2, \dots, \mathbf{q}_{N_q}] \in \mathbb{R}^{d \times N_q}$  and keys  $\mathbf{K} = [\mathbf{k}_1, \mathbf{k}_2, \dots, \mathbf{k}_{N_k}] \in \mathbb{R}^{d \times N_k}$  are first compared to

produce coefficients  $\mathbf{q}_j^\top \mathbf{k}_i / \sqrt{d}$  (they need to be normalized with the softmax function),

$$A_{i,j} = \frac{\mathbf{q}_j^\top \mathbf{k}_i / \sqrt{d}}{\sum_{i=1}^{N_k} \exp(\mathbf{q}_j^\top \mathbf{k}_i / \sqrt{d})} \quad (1)$$

The coefficients are then used to (linearly) combine values  $\mathbf{V} = [\mathbf{v}_1, \mathbf{v}_2, \dots, \mathbf{v}_{N_k}] \in \mathbb{R}^{d \times N_k}$ . We can write the output of an attention layer as follows,

$$\begin{aligned} \text{Attention}(\mathbf{Q}, \mathbf{K}, \mathbf{V}) &= [\mathbf{o}_1 \quad \mathbf{o}_2 \quad \dots \quad \mathbf{o}_{N_q}] \in \mathbb{R}^{d \times N_q} \\ &= \left[ \sum_{i=1}^{N_k} A_{i,1} \mathbf{v}_i \quad \sum_{i=1}^{N_k} A_{i,2} \mathbf{v}_i \quad \dots \quad \sum_{i=1}^{N_k} A_{i,N_q} \mathbf{v}_i \right] \end{aligned} \quad (2)$$

*Cross Attention.* Given two sets  $\mathbf{A} = [\mathbf{a}_1, \mathbf{a}_2, \dots, \mathbf{a}_{N_a}] \in \mathbb{R}^{d_a \times N_a}$  and  $\mathbf{B} = [\mathbf{b}_1, \mathbf{b}_2, \dots, \mathbf{b}_{N_b}] \in \mathbb{R}^{d_b \times N_b}$ , the query vectors  $\mathbf{Q}$  are constructed with a linear function  $\mathbf{q}(\cdot) : \mathbb{R}^{d_a} \rightarrow \mathbb{R}^d$  by taking elements of  $\mathbf{A}$  as input. Similarly, we construct  $\mathbf{K}$  and  $\mathbf{V}$  with  $\mathbf{k}(\cdot) : \mathbb{R}^{d_b} \rightarrow \mathbb{R}^d$  and  $\mathbf{v}(\cdot) : \mathbb{R}^{d_b} \rightarrow \mathbb{R}^d$ , respectively. The inputs of both  $\mathbf{k}(\cdot)$  and  $\mathbf{v}(\cdot)$  are from  $\mathbf{B}$ . Each column in the output of Eq. (2) can be written as,

$$\mathbf{o}(\mathbf{a}_j, \mathbf{B}) = \sum_{i=1}^{N_b} \mathbf{v}(\mathbf{b}_i) \cdot \frac{1}{Z(\mathbf{a}_j, \mathbf{B})} \exp(\mathbf{q}(\mathbf{a}_j)^\top \mathbf{k}(\mathbf{b}_i) / \sqrt{d}), \quad (3)$$

where  $Z(\mathbf{a}_j, \mathbf{B}) = \sum_{i=1}^{N_b} \exp(\mathbf{q}(\mathbf{a}_j)^\top \mathbf{k}(\mathbf{b}_i) / \sqrt{d})$  is a normalizing factor. The cross attention operator between two sets is,

$$\text{CrossAttn}(\mathbf{A}, \mathbf{B}) = [\mathbf{o}(\mathbf{a}_1, \mathbf{B}) \quad \mathbf{o}(\mathbf{a}_2, \mathbf{B}) \quad \dots \quad \mathbf{o}(\mathbf{a}_{N_a}, \mathbf{B})] \in \mathbb{R}^{d \times N_a} \quad (4)$$

*Self Attention.* In the case of self attention, we let the two sets be the same  $\mathbf{A} = \mathbf{B}$ ,

$$\text{SelfAttn}(\mathbf{A}) = \text{CrossAttn}(\mathbf{A}, \mathbf{A}). \quad (5)$$

## 4 LATENT REPRESENTATION FOR NEURAL FIELDS

Our representation is inspired by radial basis functions (RBFs). We will therefore describe our surface representation design using RBFs as a starting point, and how we extended them using concepts from neural fields and the transformer architecture. A continuous function can be represented with a set of weighted points in 3D using RBFs:

$$\hat{O}_{\text{RBF}}(\mathbf{x}) = \sum_{i=1}^M \lambda_i \cdot \phi(\mathbf{x}, \mathbf{x}_i) \quad (6)$$

where  $\phi(\mathbf{x}, \mathbf{x}_i)$  is a radial basis function (RBF) and typically represents the similarity (or dissimilarity) between two inputs,

$$\phi(\mathbf{x}, \mathbf{x}_i) = \phi(\|\mathbf{x} - \mathbf{x}_i\|). \quad (7)$$

Given ground-truth occupancies of  $\mathbf{x}_i$ , the values of  $\lambda_i$  can be obtained by solving a system of linear equations. In this way, we can represent the continuous function  $O(\cdot)$  as a set of  $M$  points including their corresponding weights,

$$\{\lambda_i \in \mathbb{R}, \mathbf{x}_i \in \mathbb{R}^3\}_{i=1}^M. \quad (8)$$

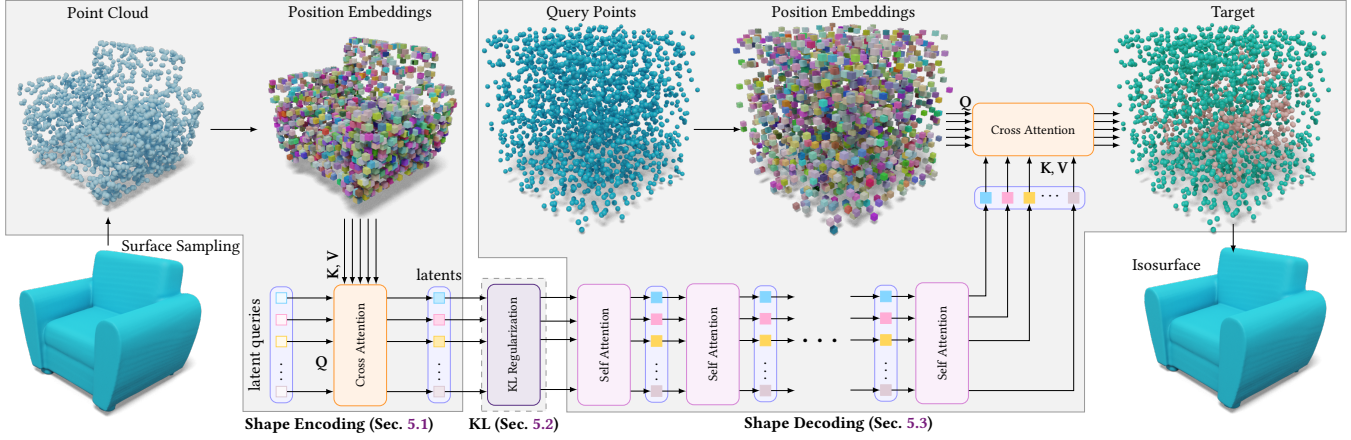


Fig. 3. **Shape autoencoding pipeline.** Given a 3D ground-truth surface mesh as the input, we first sample a point cloud that is mapped to positional embeddings and encode them into a set of latent codes through a cross-attention module (Sec. 5.1). Next, we perform (optional) compression and KL-regularization in the latent space to obtain structured and compact latent shape representations (Sec. 5.2). Finally, the self-attention is carried out to aggregate and exchange the information within the latent set. And a cross-attention module is designed to calculate the interpolation weights of query points. The interpolated feature vectors are fed into a fully connected layer for occupancy prediction (Sec. 5.3).

However, in order to retain the details of a 3d shape, we often need a very large number of points (e.g.,  $M = 80,000$  in [Carr et al. 2001]). This representation does not benefit from recent advances in representation learning and cannot compete with more compact learned representations. We therefore want to modify the representation to change it into a neural field.

One approach to neural fields is to represent each shape as a separate neural network (making the network weights of a fixed size network the representation of a shape) and train a diffusion process as hypernetwork. A second approach is to have a shared encoder-decoder network for all shapes and represent each shape as a latent computed by the encoder. We opt for the second approach, as it leads to more compact representations because it is jointly learned from all shapes in the data set and the network weights themselves do not count towards the latent representation. Such a neural field takes a tuple of coordinates  $\mathbf{x}$  and  $C$ -dimensional latent  $\mathbf{f}$  as input and outputs occupancy,

$$\hat{O}_{\text{NN}}(\mathbf{x}) = \text{NN}(\mathbf{x}, \mathbf{f}), \quad (9)$$

where  $\text{NN} : \mathbb{R}^3 \times \mathbb{R}^C \rightarrow [0, 1]$  is a neural network. A first approach was to use a single global latent  $\mathbf{f}$ , but a major limitation is the ability to encode shape details [Mescheder et al. 2019]. Some follow-up works study *coordinate-dependent* latents [Chibane et al. 2020; Peng et al. 2020; Sajjadi et al. 2022] that combine traditional data structures such as regular grids with the neural field concept. Latent vectors are arranged in a spatial data structure and then interpolated (trilinearly) to obtain the coordinate-dependent latent  $\mathbf{f}_{\mathbf{x}}$ . A recent work 3DILG [Zhang et al. 2022] proposed a sparse representation for 3D shapes, using latents  $\mathbf{f}_i$  arranged in an irregular grid at point locations  $\mathbf{x}_i$ . The final coordinate-dependent latent  $\mathbf{f}_{\mathbf{x}}$  is then estimated by kernel regression,

$$\mathbf{f}_{\mathbf{x}} = \hat{\mathcal{F}}_{\text{KN}}(\mathbf{x}) = \sum_{i=1}^M \mathbf{f}_i \cdot \frac{1}{Z(\mathbf{x}, \{\mathbf{x}_i\}_{i=1}^M)} \phi(\mathbf{x}, \mathbf{x}_i), \quad (10)$$

where  $Z(\mathbf{x}, \{\mathbf{x}_i\}_{i=1}^M) = \sum_{i=1}^M \phi(\mathbf{x}, \mathbf{x}_i)$  is a normalizing factor. Thus the representation for a 3D shape can be written as

$$\{\mathbf{f}_i \in \mathbb{R}^C, \mathbf{x}_i \in \mathbb{R}^3\}_{i=1}^M. \quad (11)$$

After that, an MLP  $\mathbb{R}^C \rightarrow [0, 1]$  is applied to project the approximated feature  $\hat{\mathcal{F}}_{\text{KN}}(\mathbf{x})$  to occupancy,

$$\hat{O}_{\text{3DILG}}(\mathbf{x}) = \text{MLP}(\hat{\mathcal{F}}_{\text{KN}}(\mathbf{x})). \quad (12)$$

*Neural networks with latent sets (proposed).* We initially explored many variations for 3D shape representation based on irregular and regular grids as well as tri-planes, frequency compositions, and other factored representations. Ultimately, we could not improve on existing irregular grids. However, we were able to achieve a significant improvement with the following change. We aim to keep the structure of an irregular grid and the interpolation, but without representing the actual spatial position explicitly. We let the network encode spatial information. Both the representations (RBF in Eq. (6) and 3DILG in Eq. (10)) are composed by two parts, **values** and **similarities**. We keep the structure of the interpolation, but eliminate explicit point coordinates and integrate cross attention from Eq. (3). The result is the following *learnable* function approximator,

$$\hat{\mathcal{F}}(\mathbf{x}) = \sum_{i=1}^M \mathbf{v}(\mathbf{f}_i) \cdot \frac{1}{Z(\mathbf{x}, \{\mathbf{f}_i\}_{i=1}^M)} e^{\mathbf{q}(\mathbf{x}) \cdot \mathbf{k}(\mathbf{f}_i) / \sqrt{d}}, \quad (13)$$

where  $Z(\mathbf{x}, \{\mathbf{f}_i\}_{i=1}^M) = \sum_{i=1}^M e^{\mathbf{q}(\mathbf{x}) \cdot \mathbf{k}(\mathbf{f}_i) / \sqrt{d}}$  is a normalizing factor. Similar to the MLP in Eq. 12, we apply a single fully connected layer to get desired occupancy values,

$$\hat{O}(\mathbf{x}) = \text{FC}(\hat{\mathcal{F}}(\mathbf{x})). \quad (14)$$

Compared to 3DILG and all other coordinate-latent-based methods, we dropped the dependency of the coordinate set  $\{\mathbf{x}_i\}_{i=1}^M$ , the new

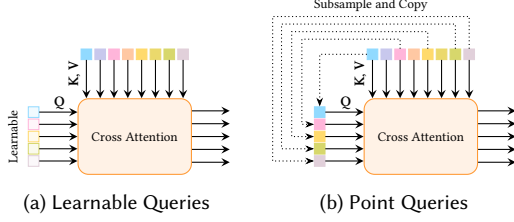


Fig. 4. **Two ways to encode a point cloud.** (a) uses a learnable query set; (b) uses a downsampled version of input point embeddings as the query set.

representation only contains a set of latents,

$$\{\mathbf{f}_i \in \mathbb{R}^C\}_{i=1}^M. \quad (15)$$

An alternative view of our proposed function approximator is to see it as cross attention between query points  $\mathbf{x}$  and a set of latents.

## 5 NETWORK ARCHITECTURE FOR SHAPE REPRESENTATION LEARNING

In this section, we will discuss how we design a variational autoencoder based on the latent representation proposed in Sec. 4. The architecture has three components discussed in the following: a 3D shape encoder, KL regularization block, and a 3D shape decoder.

### 5.1 Shape encoding

We sample the surfaces of 3D input shapes in a 3D shape dataset. This results in a point cloud of size  $N$  for each shape,  $\{\mathbf{x}_i \in \mathbb{R}^3\}_{i=1}^N$  or in matrix form  $\mathbf{X} \in \mathbb{R}^{3 \times N}$ . While the dataset used in the paper originally represents shapes as triangle meshes, our framework is directly compatible with other surface representations, such as scanned point clouds, spline surfaces, or implicit surfaces.

In order to learn representations in the form of Eq. (15), the first challenge is to aggregate the information contained in a possibly large point cloud  $\{\mathbf{x}_i\}_{i=1}^N$  into a smaller set of latent vectors  $\{\mathbf{f}_i\}_{i=1}^M$ . We design a set-to-set network to this effect.

A popular solution to this problem in previous work is to divide the large point cloud into a smaller set of patches and to learn one latent vector per patch. Although this is a very well researched and standard component in many networks, we discovered a more successful way to aggregate features from a large point cloud that is better compatible with the transformer architecture. We considered two options.

One way is to define a learnable query set. Inspired by DETR [Carion et al. 2020] and Perceiver [Jaegle et al. 2021], we use the cross attention to encode  $\mathbf{X}$ ,

$$\text{Enc}_{\text{learnable}}(\mathbf{X}) = \text{CrossAttn}(\mathbf{L}, \text{PosEmb}(\mathbf{X})) \in \mathbb{R}^{C \times M}, \quad (16)$$

where  $\mathbf{L} \in \mathbb{R}^{C \times M}$  is a *learnable query* set where each entry is  $C$ -dimensional, and  $\text{PosEmb} : \mathbb{R}^3 \rightarrow \mathbb{R}^C$  is a column-wise positional embedding function.

Another way is to utilize the point cloud itself. We first subsample the point cloud  $\mathbf{X}$  to a smaller one with furthest point sampling,  $\mathbf{X}_0 = \text{FPS}(\mathbf{X}) \in \mathbb{R}^{3 \times M}$ . The cross attention is applied to  $\mathbf{X}_0$  and  $\mathbf{X}$ ,

$$\text{Enc}_{\text{points}}(\mathbf{X}) = \text{CrossAttn}(\text{PosEmb}(\mathbf{X}_0), \text{PosEmb}(\mathbf{X})), \quad (17)$$

which can also be seen as a “partial” self attention. See Fig. 4 for an illustration of both design choices. Intuitively, the number  $M$  affects the reconstruction performance: the larger the  $M$ , the better reconstruction. However,  $M$  strongly affects the training time due to the transformer architecture, so it should not be too large. In our final model, the number of latents  $M$  is set as 512, and the number of channels  $C$  is 512 to provide a trade off between reconstruction quality and training time.

### 5.2 KL regularization block

Latent diffusion [Rombach et al. 2022] proposed to use a variational autoencoder (VAE) [Kingma and Welling 2014] to compress images. We adapt this design idea for our 3D shape representation and also regularize the latents with KL-divergence. We should note that the KL regularization is optional and only necessary for the second-stage diffusion model training. If we just want a method for surface reconstruction from point clouds, we do not need the KL regularization.

We first linear project latents to mean and variance by two network branches, respectively,

$$\begin{aligned} \text{FC}_\mu(\mathbf{f}_i) &= (\mu_{i,j})_{j \in [1, 2, \dots, C_0]} \\ \text{FC}_\sigma(\mathbf{f}_i) &= (\log \sigma_{i,j}^2)_{j \in [1, 2, \dots, C_0]} \end{aligned} \quad (18)$$

where  $\text{FC}_\mu : \mathbb{R}^C \rightarrow \mathbb{R}^{C_0}$  and  $\text{FC}_\sigma : \mathbb{R}^C \rightarrow \mathbb{R}^{C_0}$  are two linear projection layers. We use a different size of output channels  $C_0$ , where  $C_0 \ll C$ . This compression enables us to train diffusion models on smaller latents of total size  $M \cdot C_0 \ll M \cdot C$ . We can write the bottleneck of the VAE formally,  $\forall i \in [1, 2, \dots, M], j \in [1, 2, \dots, C_0]$ ,

$$z_{i,j} = \mu_{i,j} + \sigma_{i,j} \cdot \epsilon, \quad (19)$$

where  $\epsilon \sim \mathcal{N}(0, 1)$ . The KL regularization can be written as,

$$\mathcal{L}_{\text{reg}}(\{\mathbf{f}_i\}_{i=1}^M) = \frac{1}{M \cdot C_0} \sum_{i=1}^M \sum_{j=1}^{C_0} \frac{1}{2} (\mu_{i,j}^2 + \sigma_{i,j}^2 - \log \sigma_{i,j}^2). \quad (20)$$

In practice, we set the weight for KL loss as 0.001 and report the performance for different values of  $C_0$  in Sec. 8.1. Our recommended setting is  $C_0 = 32$ .

### 5.3 Shape decoding

To increase the expressivity of the network, we add a latent learning network between the two parts. Because our latents are a set of vectors, it is natural to use transformer networks here. Thus, the proposed network here is a series of self attention blocks,

$$\{\mathbf{f}_i\}_{i=1}^M \leftarrow \text{SelfAttn}^{(l)}(\{\mathbf{f}_i\}_{i=1}^M), \quad \text{for } i = 1, \dots, L. \quad (21)$$

The  $\text{SelfAttn}(\cdot)$  with a superscript  $(l)$  here means  $l$ -th block. The latents  $\{\mathbf{f}_i\}_{i=1}^M$  obtained using either Eq. (16) or Eq. (17) are fed into the self attention blocks. Given a query  $\mathbf{x}$ , the corresponding latent is interpolated using Eq. (13), and the occupancy is obtained with a fully connected layer as shown in Eq. (14).

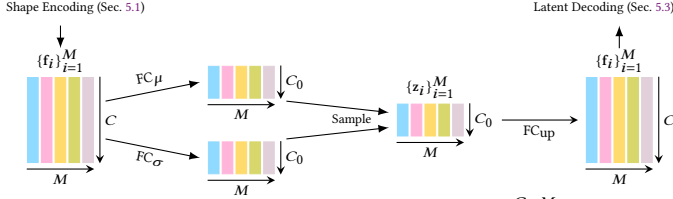


Fig. 5. **KL regularization.** Given a set of latents  $\{f_i \in \mathbb{R}^C\}_{i=1}^M$  obtained from the shape encoding in Sec. 5.1, we employ two linear projection layers  $FC_\mu, FC_\sigma$  to predict the mean and variance of a low-dimensional latent space, where a KL regularization commonly used in VAE training is applied to constrain the feature diversity. Then, we obtain smaller latents  $\{z_i \in \mathbb{R}^{C_0}\}$  of size  $M \cdot C_0 \ll M \cdot C$  via reparametrization sampling. Finally, the compressed latents are mapped back to the original space by  $FC_{up}$  to obtain a higher dimensionality for the shape decoding in Sec. 5.3.

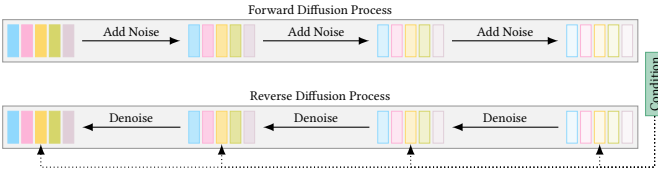


Fig. 6. **Latent set diffusion models.** The diffusion model operates on compressed 3D shapes in the form of a regularized set of latent vectors  $\{z_i\}_{i=1}^M$ .

*Loss.* We optimize the binary cross entropy loss between our approximated function and the ground-truth indicator function as in prior works [Mescheder et al. 2019].

$$\mathcal{L}_{recon}(\{f_i\}_{i=1}^M, \mathcal{O}) = \mathbb{E}_{\mathbf{x} \in \mathbb{R}^3} [\text{BCE}(\hat{\mathcal{O}}(\mathbf{x}), \mathcal{O}(\mathbf{x}))]. \quad (22)$$

*Surface reconstruction.* We sample query points in a grid of resolution  $128^3$ . The final surface is reconstructed with Marching Cubes [Lorensen and Cline 1987].

## 6 SHAPE GENERATION

Our proposed diffusion model combines design decisions from latent diffusion (the idea of the compressed latent space), EDM [Karras et al. 2022] (most of the training details), and our shape representation design (the architecture is based on attention and self-attention instead of convolution).

We train diffusion models in the latent space, *i.e.*, the bottleneck in Eq. (19). Following the diffusion formulation in EDM [Karras et al. 2022], our denoising objective is

$$\mathbb{E}_{\mathbf{n}_i \sim \mathcal{N}(0, \sigma^2 \mathbf{I})} \frac{1}{M} \sum_{i=1}^M \left\| \text{Denoiser}(\{z_i + \mathbf{n}_i\}_{i=1}^M, \sigma, C)_i - z_i \right\|_2^2, \quad (23)$$

where  $\text{Denoiser}(\cdot, \cdot, \cdot)$  is our denoising neural network,  $\sigma$  is the noise level, and  $C$  is the optional conditional information (*e.g.*, categories, images, partial point clouds and texts). We denote the corresponding output of  $z_i + \mathbf{n}_i$  with the subscript  $i$ , *i.e.*  $\text{Denoiser}(\cdot, \cdot, \cdot)_i$ . We should minimize the loss for every noise level  $\sigma$ . The sampling is done by solving ordinary/stochastic differential equations (ODE/SDE). See Fig. 6 for an illustration and EDM [Karras et al. 2022] for a detailed description for both the forward (training) and reverse (sampling) process.

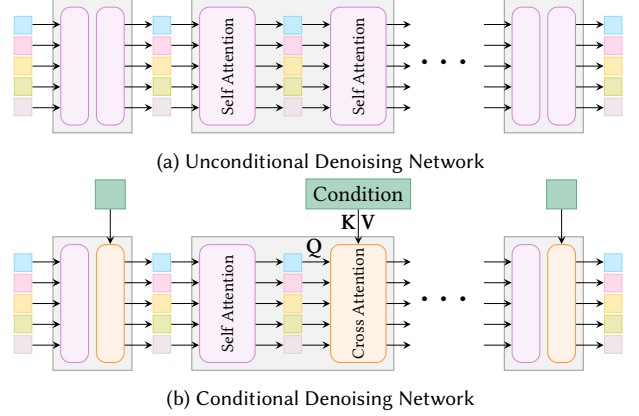


Fig. 7. **Denoising network.** Our denoising network is composed of several denoising layers (a box in the figure denotes a layer). The denoising layer for unconditional generation contains two sequential self attention blocks. The denoising layer for conditional generation contains a self attention and a cross attention block. The cross attention is for injecting condition information such as categories, images or partial point clouds.

The function  $\text{Denoiser}(\cdot, \cdot, \cdot)$  is a set denoising network (set-to-set function). The network can be easily modeled by a self-attention transformer. Each layer consists of two attention blocks. The first one is a self attention for attentive learning of the latent set. The second one is for injecting the condition information  $C$  (Fig. 7 (b)) as in prior works [Rombach et al. 2022]. For simple information like categories,  $C$  is a learnable embedding vector (*e.g.*, 55 different embedding vectors for 55 categories). For a single-view image, we use ResNet-18 [He et al. 2016] as the context encoder to extract a global feature vector as condition  $C$ . For text conditioning, we use BERT [Devlin et al. 2018] to learn a global feature vector as  $C$ . For partial point clouds, we use the shape encoder introduced in Sec. 5.1 to obtain a set of latent embeddings as  $C$ . In the case of unconditional generation, the cross attention degrades to self attention (Fig. 7 (a)).

## 7 EXPERIMENTAL SETUP

We use the dataset of ShapeNet-v2 [Chang et al. 2015] as a benchmark, containing 55 categories of man-made objects. We use the training/val splits in [Zhang et al. 2022]. We preprocess shapes as in [Mescheder et al. 2019]. Each shape is first converted to a watertight mesh, and then normalized to its bounding box, from which we further sample a dense surface point cloud of size 500,000. To learn the neural fields, we randomly sample 500,000 points with occupancies in the 3D space, and 500,000 points with occupancies in the near surface region. For the single-view object reconstruction, we use the 2D rendering dataset provided by 3D-R2N2 [Choy et al. 2016], where each shape is rendered into RGB images of size of  $224 \times 224$  from 24 random viewpoints. For text-driven shape generation, we use the text prompts of ShapeGlot [Achlioptas et al. 2019]. For data preprocess of shape completion training, we create partial point clouds by sampling point cloud patches.

Table 3. **Shape autoencoding (surface reconstruction from point clouds) on ShapeNet.** We show averaged metrics on all 55 categories and individual metrics for the 7 largest categories. We compare with existing representative methods, **OccNet** (global latent), **ConvOccNet** (local latent grid), **IF-Net** (multiscale local latent grid), and **3DILG** (irregular latent grid). For our method, we show two different designs. The column **Learned Queries** shows results of using Eq. (16), while the column **Point Queries** means we are using a subsampled point set as queries in Eq. (17). The results of **Point Queries** are generally better than **Learned Queries**. This is expected because input-dependent queries (**Point Queries**) are better than fixed queries (**Learned Queries**).

|           |                 | OccNet | ConvOccNet | IF-Net | 3DILG        | Ours            |               |
|-----------|-----------------|--------|------------|--------|--------------|-----------------|---------------|
|           |                 |        |            |        |              | Learned Queries | Point Queries |
| IoU ↑     | table           | 0.823  | 0.847      | 0.901  | 0.963        | 0.965           | <b>0.971</b>  |
|           | car             | 0.911  | 0.921      | 0.952  | 0.961        | 0.966           | <b>0.969</b>  |
|           | chair           | 0.803  | 0.856      | 0.927  | 0.950        | 0.957           | <b>0.964</b>  |
|           | airplane        | 0.835  | 0.881      | 0.937  | 0.952        | 0.962           | <b>0.969</b>  |
|           | sofa            | 0.894  | 0.930      | 0.960  | 0.975        | 0.975           | <b>0.982</b>  |
|           | rifle           | 0.755  | 0.871      | 0.914  | 0.938        | 0.947           | <b>0.960</b>  |
|           | lamp            | 0.735  | 0.859      | 0.914  | 0.926        | 0.931           | <b>0.956</b>  |
|           | mean (selected) | 0.822  | 0.881      | 0.929  | 0.952        | 0.957           | <b>0.967</b>  |
|           | mean (all)      | 0.825  | 0.888      | 0.934  | 0.953        | 0.955           | <b>0.965</b>  |
| Chamfer ↓ | table           | 0.041  | 0.036      | 0.029  | <b>0.026</b> | <b>0.026</b>    | <b>0.026</b>  |
|           | car             | 0.082  | 0.083      | 0.067  | 0.066        | <b>0.062</b>    | <b>0.062</b>  |
|           | chair           | 0.058  | 0.044      | 0.031  | 0.029        | 0.028           | <b>0.027</b>  |
|           | airplane        | 0.037  | 0.028      | 0.020  | 0.019        | 0.018           | <b>0.017</b>  |
|           | sofa            | 0.051  | 0.042      | 0.032  | 0.030        | 0.030           | <b>0.029</b>  |
|           | rifle           | 0.046  | 0.025      | 0.018  | 0.017        | 0.016           | <b>0.014</b>  |
|           | lamp            | 0.090  | 0.050      | 0.038  | 0.036        | 0.035           | <b>0.032</b>  |
|           | mean (selected) | 0.058  | 0.040      | 0.034  | 0.032        | 0.031           | <b>0.030</b>  |
|           | mean (all)      | 0.072  | 0.052      | 0.041  | 0.040        | 0.039           | <b>0.038</b>  |
| F-Score ↑ | table           | 0.961  | 0.982      | 0.998  | <b>0.999</b> | <b>0.999</b>    | <b>0.999</b>  |
|           | car             | 0.830  | 0.852      | 0.888  | 0.892        | 0.898           | <b>0.899</b>  |
|           | chair           | 0.890  | 0.943      | 0.990  | 0.992        | 0.994           | <b>0.997</b>  |
|           | airplane        | 0.948  | 0.982      | 0.994  | 0.993        | 0.994           | <b>0.995</b>  |
|           | sofa            | 0.918  | 0.967      | 0.988  | 0.986        | 0.986           | <b>0.990</b>  |
|           | rifle           | 0.922  | 0.987      | 0.998  | 0.997        | 0.998           | <b>0.999</b>  |
|           | lamp            | 0.820  | 0.945      | 0.970  | 0.971        | 0.970           | <b>0.975</b>  |
|           | mean (selected) | 0.898  | 0.951      | 0.975  | 0.976        | 0.977           | <b>0.979</b>  |
|           | mean (all)      | 0.858  | 0.933      | 0.967  | 0.966        | 0.966           | <b>0.970</b>  |

## 7.1 Baselines

For shape auto-encoding, we conduct experiments against state-of-the-art methods for implicit surface reconstruction from point clouds. We use OccNet [Mescheder et al. 2019], ConvOccNet [Peng et al. 2020], IF-Net [Chibane et al. 2020], and 3DILG [Zhang et al. 2022] as baselines. The OccNet is the first work of learning neural fields from a single global latent vector. ConvOccNet and IF-Net learn local neural fields based on latent vectors arranged in a regular grid, while 3DILG uses latent vectors on an irregular grid.

For 3D shape generation, we compare against recent state-of-the-art generative models, including PVD [Zhou et al. 2021], 3DILG [Zhang et al. 2022], and NeuralWavelet [Hui et al. 2022]. PVD is a diffusion model for 3D point cloud generation, and 3DILG utilizes autoregressive models. NeuralWavelet utilized diffusion models in the frequency domain of shapes.

## 7.2 Evaluation metrics

To evaluate the reconstruction accuracy of shape auto-encoding from point clouds, we adopt Chamfer distance, volumetric Intersection-over-Union (IoU), and F-score as primary evaluation metrics. IoU is computed based on the occupancy predictions of 50k querying points sampled in 3D space. Chamfer distance and F-score are calculated between two sampled point clouds with the size of 50k respectively from reconstructed and ground-truth surfaces. For IoU and F-score, higher is better, while for Chamfer, lower is better.

To measure the mesh quality of unconditional and conditional shape generation, we follow [Ibing et al. 2021; Shue et al. 2022; Zhang et al. 2022] to adapt the Fréchet Inception Distance (FID) and Kernel Inception Distance (KID) commonly used to assess the image generative models to rendered images of 3d shapes. To calculate FID and KID of rendered images, we render each shape from 10 viewpoints. The metrics are named as **Rendering-FID** and **Rendering-KID**.

The Rendering-FID is defined as,

$$\text{Rendering-FID} = \|\mu_g - \mu_r\| + \text{Tr} \left( \Sigma_g + \Sigma_r - 2(\Sigma_g \Sigma_r)^{1/2} \right) \quad (24)$$



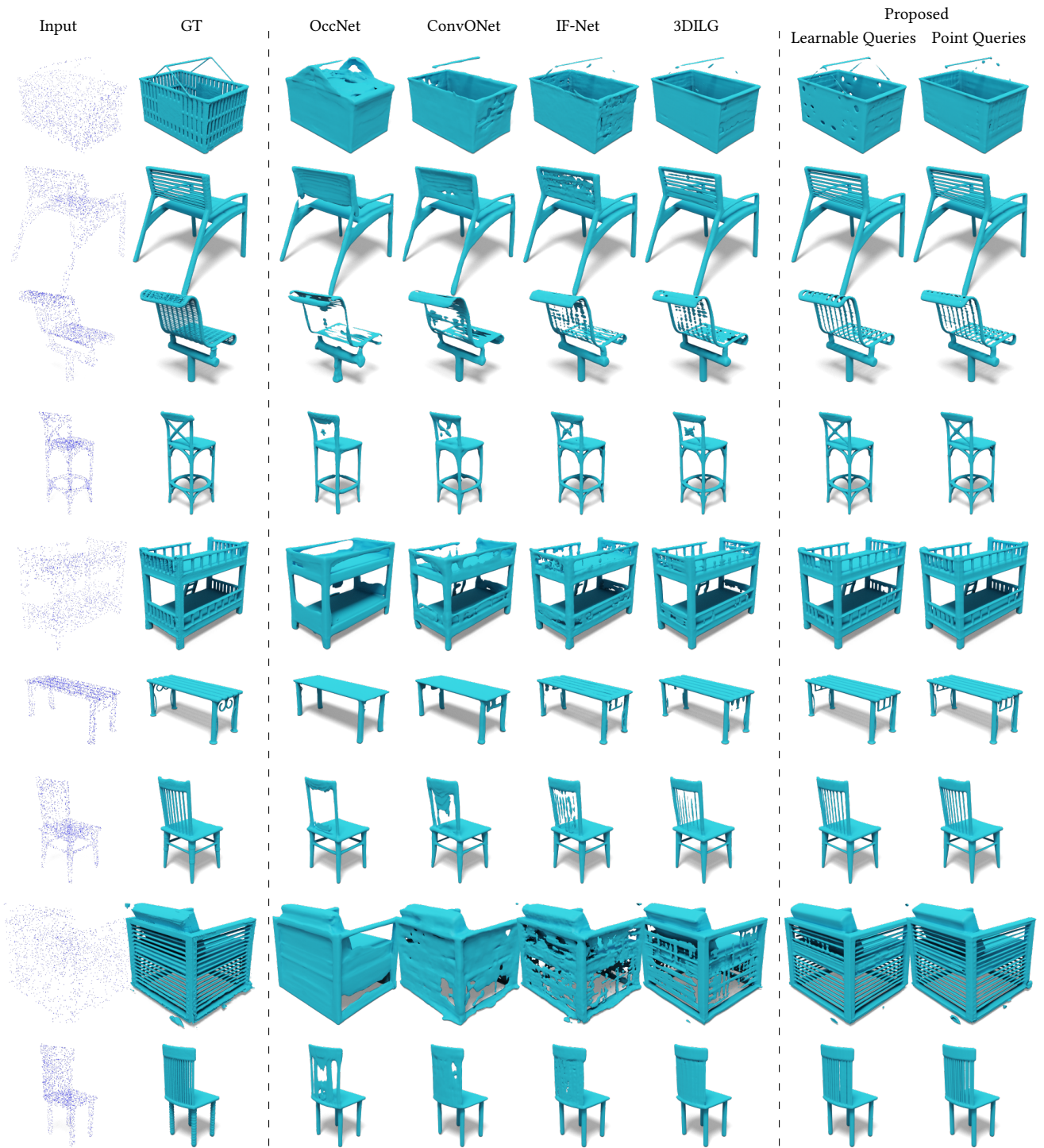


Fig. 8. Visualization of shape autoencoding results (surface reconstruction from point clouds from ShapeNet).

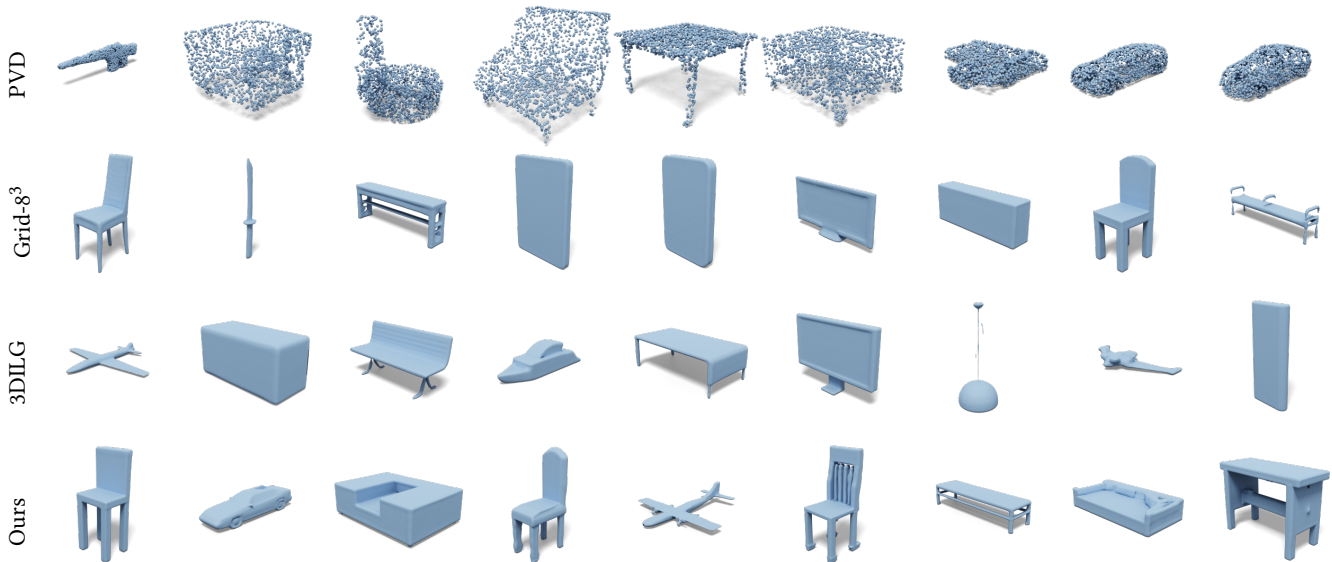


Fig. 9. **Unconditional generation.** All models are trained on full ShapeNet.

where  $g$  and  $r$  denotes the generated and training datasets respectively.  $\mu$  and  $\Sigma$  are the statistical mean and covariance matrix of the feature distribution extracted by the Inception network.

The Rendering-KID is defined as,

$$\text{Rendering-KID} = \text{MMD} \left( \frac{1}{|\mathcal{R}|} \sum_{\mathbf{x} \in \mathcal{R}} \max_{\mathbf{y} \in \mathcal{G}} D(\mathbf{x}, \mathbf{y}) \right)^2 \quad (25)$$

where  $D(\mathbf{x}, \mathbf{y})$  is a polynomial kernel function to evaluate the similarity of two samples.  $\mathcal{G}$  and  $\mathcal{R}$  are feature distributions of generated set and reference set, respectively. The function  $\text{MMD}(\cdot)$  is Maximum Mean Discrepancy. However, the rendering-based FID and KID are essentially designed to understand 3D shapes from 2D images. Thus, they have the inherent issue of not accurately understanding shape compositions in the 3D world. To compensate their drawbacks, we also adapt the FID and KID to 3D shapes directly. For each generated or ground-truth shape, we sample 4096 points (with normals) from the surface mesh and then feed them into a pre-trained PointNet++ [Qi et al. 2017b] to extract a global latent vector, representing the global structure of the 3D shape. The PointNet++ is first pretrained on shape classification on ShapeNet-55. As we use point clouds, we call the FID and KID for 3D shapes as Fréchet PointNet++ Distance (FPD) and Kernel PointNet++ Distance (KPD). The two metrics are defined similarly as in Eq. (24) and Eq. (25), except that the features are extracted from a PointNet++ network.

### 7.3 Implementation

For the shape auto-encoder, we use the point cloud of size 2048 as input. At each iteration, we individually sample 1024 query points from the bounding volume  $([-1, 1]^3)$  and the other 1024 points from near surface region for the occupancy values prediction. The shape auto-encoder is trained on 8 A100, with batch size of 512 for  $T = 1,600$  epochs. The learning rate is linearly increased to

$lr_{\max} = 5e - 5$  in the first  $t_0 = 80$  epochs, and then gradually decreased using the cosine decay schedule  $lr_{\max} * 0.5^{1+\cos(\frac{t-t_0}{T-t_0})}$  until reaching the minimum value of  $1e - 6$ . The diffusion models are trained on 4 A100 with batch size of 256 for  $T = 8,000$  epochs. The learning rate is linearly increased to  $lr_{\max} = 1e - 4$  in the first  $t_0 = 800$  epochs, and then gradually decreased using the above mentioned decay schedule until reaching  $1e - 6$ . We use the default settings for the hyperparameters of EDM [Karras et al. 2022]. During sampling, we obtain the final latent set via only 18 denoising steps.

## 8 RESULTS

We present our results for multiple applications: 1) shape auto-encoding, 2) unconditional generation, 3) category-conditioned generation, 4) text-conditioned generation, 5) shape completion, 6) image-conditioned generation. Finally, we perform a shape novelty analysis to validate that we are not overfitting to the dataset.

### 8.1 Shape Auto-Encoding

We show the quantitative results in Tab. 3 for a deterministic autoencoder without the KL block described in Sec. 5.2. In particular, we show results for the largest 7 categories as well as averaged results over the categories. The two design choices of shape encoding described in Sec. 5.1 are also investigated. The case of using the subsampled point cloud as queries is better than learnable queries in all categories. Thus we use subsampled point clouds in our later experiments. The visualization of reconstruction results can be found in Fig. 8. We visualize some extremely difficult shapes from the datasets (test split). These shapes often contain some thin structures. However, our method still performs well.

Both our method and the competitor 3DILG use transformer as the main backbone. However, we differ in nature. 1) For encoding, 3DILG uses KNN to aggregate local information and we use cross

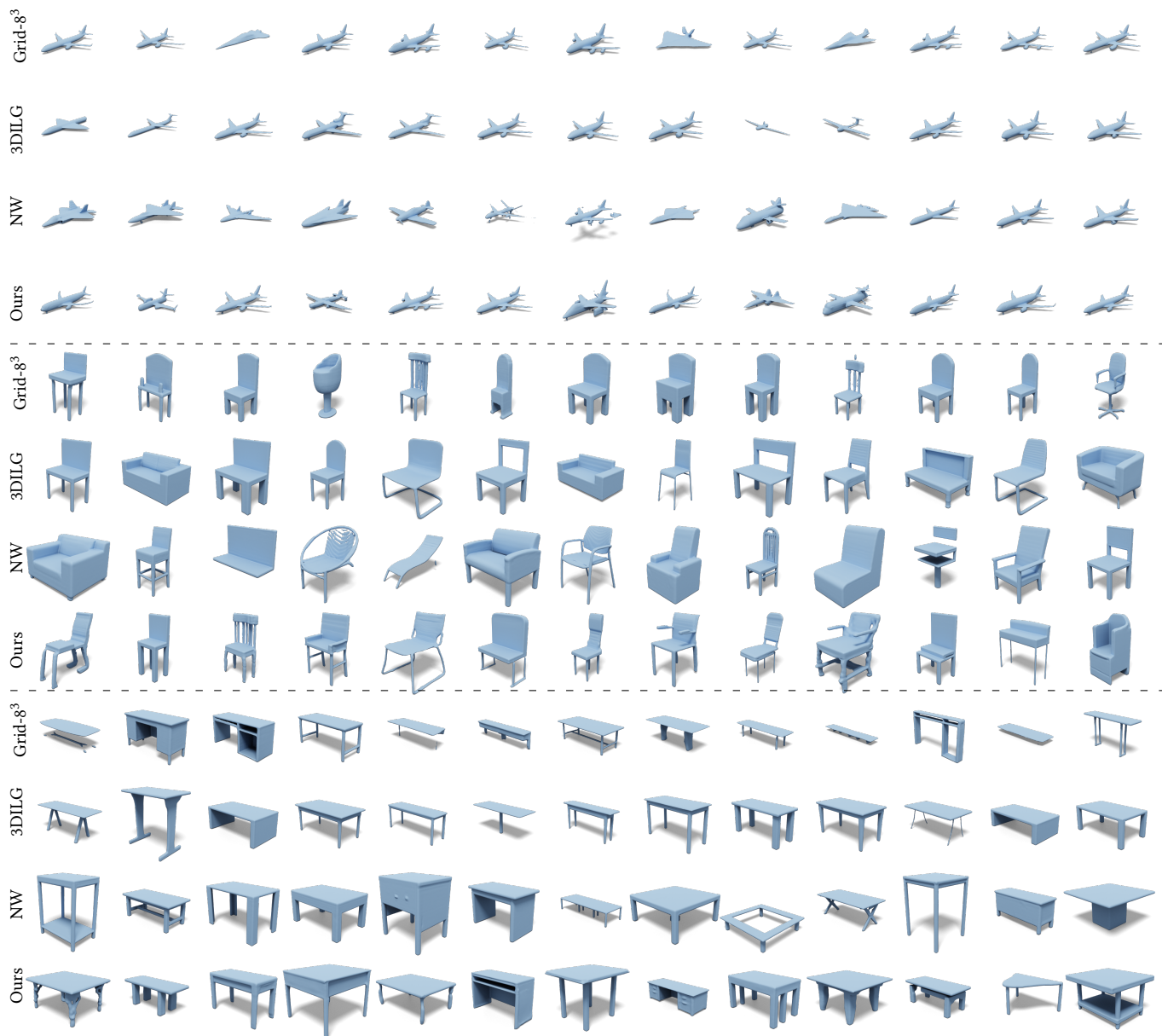


Fig. 10. **Category-conditional generation.** From top to bottom, we show category (*airplane, chair, table*) conditioned generation results.

attention. KNN manually selects neighboring points according to spatial similarities (distances) while cross attention learns the similarities on the go. 2) 3DILG uses a set of points and one latent per point. Our representation only contains a set of latents. This simplification makes the second-stage generative model training easier. 3) For decoding, 3DILG applies spatial interpolation and we use interpolation in feature space. The used cross attention can be seen as learnable interpolation. This gives us more flexibility.

The numerical results for the reconstruction are significant. The maximum achievable number for the metrics IoU and F1 is 1. The improvement has to be interpreted in how much closer we get to 1. The visualizations also highlight the improvement.

*Ablation study of the number of latents.* The number  $M$  is the number of latent vectors used in the network. Intuitively, a larger  $M$  leads to a better reconstruction. We show results of  $M$  in Tab. 4. Thus, in all of our experiments,  $M$  is set to 512. We are limited by computation time to work with larger  $M$ .

*Ablation study of the KL block.* We described the KL block in Sec. 5.2 that leads to additional compression. In addition, this block changes the deterministic shape encoding into a variational autoencoder. The introduced hyperparameter is  $C_0$ . A smaller  $C_0$  leads to a higher compression rate. The choice of  $C_0$  is ablated in Tab. 5. Clearly, larger  $C_0$  gives better results. The reconstruction results of  $C_0 = 8, 16, 32, 64$  are very close. However, they differ significantly in the second stage, because a larger latent size could make the training of diffusion models more difficult. This result is very encouraging for our model, because it indicates that aggressively increasing the compression in the KL block does not decrease reconstruction performance too much. We can also see that compressing with the KL block by decreasing  $C_0$  is much better than compressing using fewer latent vectors  $M$ .

## 8.2 Unconditional Shape Generation

*Comparison with surface generation.* We evaluate the task of unconditional shape generation with the proposed metrics in Tab. 6. We also compared our method with a baseline method proposed in [Zhang et al. 2022]. The method is called Grid-8<sup>3</sup> because the latent grid size is 8<sup>3</sup>, which is exactly the same as in AutoSDF [Mittal et al. 2022]. The table also shows the results of different  $C_0$ . Our results are best when  $C_0 = 32$  in all metrics. When  $C_0 = 64$  the results become worse. This also aligns with our conjecture that a larger latent size makes the training more difficult.

*Comparison with point cloud generation.* Additionally, we compare our method with PVD [Zhou et al. 2021] which is a point cloud diffusion method. We re-train PVD using the official released code on our preprocessed dataset and splits. We use the same evaluation protocol as before but with one major difference. Since PVD can only generate point clouds without normals, we use another pretrained PointNet++ (without normals) as the feature extractor to calculate Surface-FPD and Surface-KPD. The Tab. 7 shows we can beat PVD by a large margin. Additionally, we also show the metrics calculated on rendered images. Visualization of generated results can be found in Fig. 9.

## 8.3 Category-conditioned generation

We train a category-conditioned generation model using our method. We evaluate our models in Tab. 8. We should note that the competitor method NeuralWavelet [Hui et al. 2022] trains models for categories separately; thus, NeuralWavelet is not a true category-conditioned model. We also visualize some results (*airplane, chair, and table*) in Fig. 10. Our training is more challenging, as we train on a dataset that is an order of magnitude larger and we train for all classes jointly. While NeuralWavelet already has good results, the joint training is necessary / beneficial for many subsequent applications.

Additionally, we show evaluation metrics and more competitor methods in Tab. 9. First, we use precision and recall (P&R) [Sajjadi et al. 2018] to quantify the percentage of generated samples that are similar to training and the percentage of training data that can be generated, respectively. 3DILG, NeuralWavelet, and our method, can achieve high precision which means they can generate similar shapes to training. However, our method also shows significantly

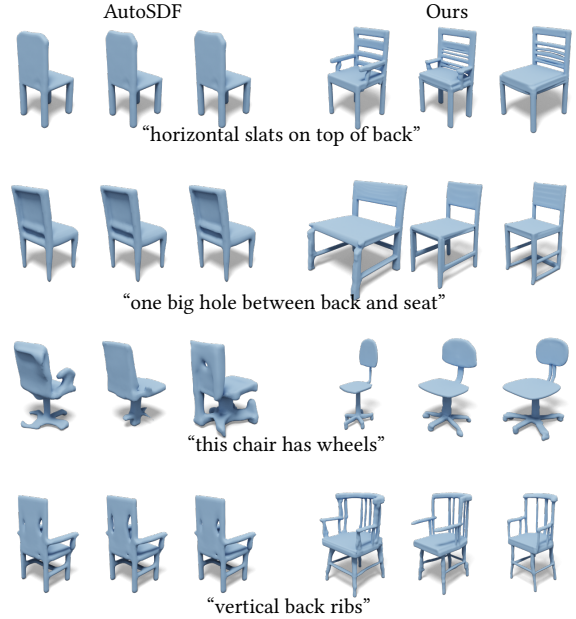


Fig. 11. **Text conditioned generation.** For each text prompt, we generate 3 shapes. Our results (**Right**) are compared with AutoSDF (**Left**).

better recall, which means our method can generate a higher percentage of the training data. For 3DShapeGen and AutoSDF, both precision and recall are low compared to other methods. Second, we show other metrics based on point cloud distances (CD and EMD) [Achlioptas et al. 2018]. The smaller the better for MMD and the larger the better for COV. These metrics are often used to evaluate point cloud generation.

## 8.4 Text-conditioned generation

The results of our text-conditioned generation model can be found in Fig. 11. Since the model is a probabilistic model, we can sample shapes given a text prompt. The results are very encouraging and they constitute the first demonstration of text-conditioned 3D shape generation using diffusion models. To the best of our knowledge, there are no published competing methods at the point of submitting this work.

## 8.5 Probabilistic shape completion

We also extend our diffusion model for probabilistic shape completion by using a partial point cloud as conditioning input. The comparison against ShapeFormer [Yan et al. 2022] is depicted in Fig. 12. As seen, our latent set diffusion can predict more accurate completion, and we also have the ability to achieve more diverse generations.

## 8.6 Image-conditioned shape generation.

We also provide comparisons on the task of single-view 3D object reconstruction in Fig. 13. Compared to other deterministic methods including OccNet [Mescheder et al. 2019] and IM-Net [Chen and Zhang 2019], our latent set diffusion can not only reconstruct more accurate surface details, (e.g. long rods and tiny holes in the back),

Table 4. **Ablation study** for different number of latents  $M$  for shape autoencoding

|                      | $M = 512$    | $M = 256$ | $M = 128$ | $M = 64$ |
|----------------------|--------------|-----------|-----------|----------|
| IoU $\uparrow$       | <b>0.965</b> | 0.956     | 0.940     | 0.916    |
| Chamfer $\downarrow$ | <b>0.038</b> | 0.039     | 0.043     | 0.049    |
| F-Score $\uparrow$   | <b>0.970</b> | 0.965     | 0.953     | 0.929    |

Table 5. **Ablation study** for different number of channels  $C_0$  for shape (variational) autoencoding.

|                      | $C_0 = 1$ | $C_0 = 2$ | $C_0 = 4$    | $C_0 = 8$    | $C_0 = 16$   | $C_0 = 32$   | $C_0 = 64$   |
|----------------------|-----------|-----------|--------------|--------------|--------------|--------------|--------------|
| IoU $\uparrow$       | 0.727     | 0.816     | 0.957        | 0.960        | 0.962        | 0.963        | <b>0.964</b> |
| Chamfer $\downarrow$ | 0.133     | 0.087     | <b>0.038</b> | <b>0.038</b> | <b>0.038</b> | <b>0.038</b> | <b>0.038</b> |
| F-Score $\uparrow$   | 0.703     | 0.815     | 0.967        | 0.967        | <b>0.970</b> | 0.969        | <b>0.970</b> |

Table 6. **Unconditional generation** on full ShapeNet.

|  | Grid-8 <sup>3</sup> | 3DILG | Ours      |            |              |            |
|--|---------------------|-------|-----------|------------|--------------|------------|
|  |                     |       | $C_0 = 8$ | $C_0 = 16$ | $C_0 = 32$   | $C_0 = 64$ |
| Surface-FPD $\downarrow$                     | 4.03                | 1.89  | 2.71      | 1.87       | <b>0.76</b>  | 0.97       |
| Surface-KPD ( $\times 10^3$ ) $\downarrow$   | 6.15                | 2.17  | 3.48      | 2.42       | <b>0.66</b>  | 1.11       |
| Rendering-FID $\downarrow$                   | 32.78               | 24.83 | 28.25     | 27.26      | <b>17.08</b> | 24.24      |
| Rendering-KID ( $\times 10^3$ ) $\downarrow$ | 14.12               | 10.51 | 14.60     | 19.37      | <b>6.75</b>  | 11.76      |

Table 7. **Unconditional generation** on full ShapeNet.

|  | PVD    | Ours         |
|--|--------|--------------|
| Surface-FPD $\downarrow$                     | 2.33   | <b>0.63</b>  |
| Surface-KPD ( $\times 10^3$ ) $\downarrow$   | 2.65   | <b>0.53</b>  |
| Rendering-FID $\downarrow$                   | 270.64 | <b>17.08</b> |
| Rendering-KID ( $\times 10^3$ ) $\downarrow$ | 281.54 | <b>6.75</b>  |

Table 8. **Category conditioned generation.** *NW* is short for NeuralWavelet. The dash sign “-” means the method NeuralWavelet does not release models trained on these categories.

|                               | airplane |             |      | chair |      |             | table |             |      | car   |    |             | sofa  |    |             |
|-------------------------------|----------|-------------|------|-------|------|-------------|-------|-------------|------|-------|----|-------------|-------|----|-------------|
|                               | 3DILG    | NW          | Ours | 3DILG | NW   | Ours        | 3DILG | NW          | Ours | 3DILG | NW | Ours        | 3DILG | NW | Ours        |
| Surface-FID                   | 0.71     | <b>0.38</b> | 0.62 | 0.96  | 1.14 | <b>0.76</b> | 2.10  | <b>1.12</b> | 1.19 | 2.93  | -  | <b>2.04</b> | 1.83  | -  | <b>0.77</b> |
| Surface-KID ( $\times 10^3$ ) | 0.81     | <b>0.53</b> | 0.83 | 1.21  | 1.50 | <b>0.70</b> | 3.84  | <b>1.55</b> | 1.87 | 7.35  | -  | <b>3.90</b> | 3.36  | -  | <b>0.70</b> |

Table 9. **Category conditioned generation II.** We show results for additional metrics and additional methods for category conditioned generation.

|  | chair       |            |         |             |              | table       |            |         |       |              |
|--|-------------|------------|---------|-------------|--------------|-------------|------------|---------|-------|--------------|
|  | 3DILG       | 3DShapeGen | AutoSDF | NW          | Ours         | 3DILG       | 3DShapeGen | AutoSDF | NW    | Ours         |
| Precision $\uparrow$                   | 0.87        | 0.56       | 0.42    | <b>0.89</b> | 0.86         | <b>0.85</b> | 0.64       | 0.64    | 0.83  | 0.83         |
| Recall $\uparrow$                      | 0.65        | 0.45       | 0.23    | 0.57        | <b>0.86</b>  | 0.59        | 0.52       | 0.69    | 0.68  | <b>0.89</b>  |
| MMD-CD ( $\times 10^2$ ) $\downarrow$  | <b>1.78</b> | 2.14       | 7.27    | 2.14        | <b>1.78</b>  | 2.85        | 2.65       | 2.77    | 2.68  | <b>2.38</b>  |
| MMD-EMD ( $\times 10^2$ ) $\downarrow$ | 9.43        | 10.55      | 19.57   | 11.15       | <b>9.41</b>  | 11.02       | 9.53       | 9.63    | 9.60  | <b>8.81</b>  |
| COV-CD ( $\times 10^2$ ) $\uparrow$    | 31.95       | 28.01      | 6.31    | 29.19       | <b>37.48</b> | 18.54       | 23.61      | 21.55   | 21.71 | <b>25.83</b> |
| COV-EMD ( $\times 10^2$ ) $\uparrow$   | 36.29       | 36.69      | 18.34   | 34.91       | <b>45.36</b> | 27.73       | 43.26      | 29.16   | 30.74 | <b>43.58</b> |

but also support multi-modal prediction, which is a desired property to deal with severe occlusions.

### 8.7 Shape novelty analysis

We use shape retrieval to demonstrate that we are not simply overfitting to the training set. Given a generated shape, we measure the Chamfer distance between it and training shapes. The visualization of retrieved shapes can be found in Fig. 14. Clearly, the model can synthesize new shapes with realistic structures.

### 8.8 Limitations

While our method shows convincing results on a variety of tasks, our design choices also have drawbacks that we would like to discuss. For instance, we require a two stage training strategy. While this leads to improved performance in terms of generation quality, training the first stage is more time consuming than relying on manually-designed features such as wavelets [Hui et al. 2022]. In addition, the first stage might require retraining if the shape data in

consideration changes, and for the second stage – the core of our diffusion architecture – training time is also relatively high. Overall, we believe that there is significant potential for future research avenues to speed up training, in particular, in the context of diffusion models.

## 9 CONCLUSION

We have introduced 3DShape2VecSet, a novel shape representation for neural fields that is tailored to generative diffusion models. To this end, we combine ideas from radial basis functions, previous neural field architectures, variational autoencoding, as well as cross attention and self-attention to design a learnable representation. Our shape representation can take a variety of inputs including triangle meshes and point clouds and encode 3D shapes as neural fields on top of a set of latent vectors. As a result, our method demonstrates improved performance in 3D shape encoding and 3D

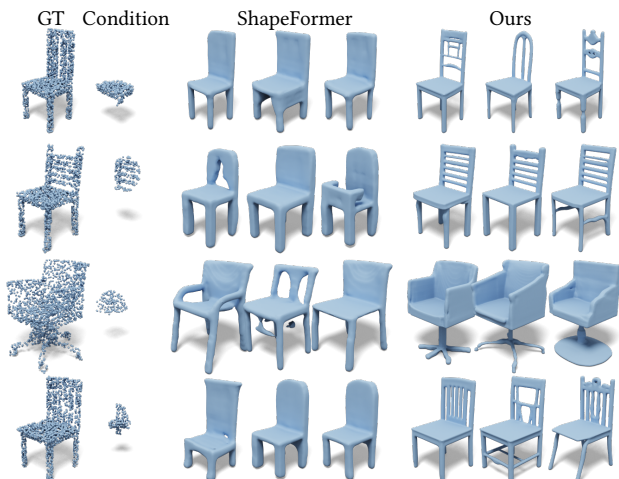


Fig. 12. **Point cloud conditioned generation.** We show three generated results given a partial cloud. The ground-truth point cloud and the partial point cloud used as condition are shown in **Left**. We compare our results (**Right**) with ShapeFormer (**Middle**).

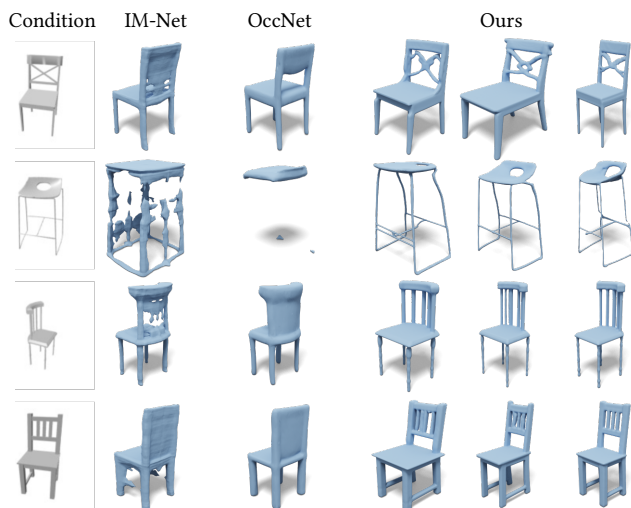


Fig. 13. **Image conditioned generation.** In the **left** column we show the condition image. In the **middle** we show results obtained by the method IM-Net and OccNet. Our generated results are shown on the **right**.



Fig. 14. **Shape generation novelty.** For a generated shape, we retrieve the top-1 similar shape in the training set. The similarity is measured using Chamfer distance of sampled surface point clouds. In each pair, we show the retrieved shape (**left**) and the generated shape (**right**). The generated shapes are from our category-conditioned generation results.

shape generative modeling tasks, including unconditioned generation, category-conditioned generation, text-conditioned generation, point-cloud completion, and image-conditioned generation.

In future work, we see many exciting possibilities. Most importantly, we believe that our model further advances the state of the art in point cloud and shape processing on a large variety of tasks. In particular, we would like to employ the network architecture of 3DShape2VecSet to tackle the problem of surface reconstruction from scanned point clouds. In addition, we can see many applications for content-creation tasks, for example 3D shape generation of textured models along with their material properties. Finally, we would like to explore editing and manipulation tasks leveraging pretrained diffusion models for prompt to prompt shape editing, leveraging the recent advances in image diffusion models.

## ACKNOWLEDGMENTS

We would like to acknowledge Anna Frühstück for helping with figures and the video voiceover. This work was supported by the SDAIA-KAUST Center of Excellence in Data Science and Artificial Intelligence (SDAIA-KAUST AI) as well as the ERC Starting Grant Scan2CAD (804724).

## REFERENCES

- Panos Achlioptas, Olga Diamanti, Ioannis Mitliagkas, and Leonidas Guibas. 2018. Learning representations and generative models for 3d point clouds. In *International conference on machine learning*. PMLR, 40–49.
- Panos Achlioptas, Judy Fan, Robert Hawkins, Noah Goodman, and Leonidas J Guibas. 2019. ShapeGlot: Learning language for shape differentiation. In *Proceedings of the IEEE/CVF International Conference on Computer Vision*, 8938–8947.
- Alexandre Boulch and Renaud Marlet. 2022. POCO: Point convolution for surface reconstruction. In *Proceedings of the IEEE/CVF Conference on Computer Vision and Pattern Recognition*, 6302–6314.
- Andrew Brock, Theodore Lim, James M Ritchie, and Nick Weston. 2016. Generative and discriminative voxel modeling with convolutional neural networks. *arXiv preprint arXiv:1608.04236* (2016).
- Nicolas Carion, Francisco Massa, Gabriel Synnaeve, Nicolas Usunier, Alexander Kirillov, and Sergey Zagoruyko. 2020. End-to-end object detection with transformers. In *European conference on computer vision*. Springer, 213–229.
- Jonathan C Carr, Richard K Beatson, Jon B Cherrie, Tim J Mitchell, W Richard Fright, Bruce C McCallum, and Tim R Evans. 2001. Reconstruction and representation of 3D objects with radial basis functions. In *Proceedings of the 28th annual conference on Computer graphics and interactive techniques*, 67–76.
- Rohan Chabra, Jan E Lenssen, Eddy Ilg, Tanner Schmidt, Julian Straub, Steven Lovegrove, and Richard Newcombe. 2020. Deep local shapes: Learning local sdf priors for detailed 3d reconstruction. In *European Conference on Computer Vision*. Springer, 608–625.
- Eric R. Chan, Connor Z. Lin, Matthew A. Chan, Koki Nagano, Boxiao Pan, Shalini De Mello, Orazio Gallo, Leonidas Guibas, Jonathan Tremblay, Sameh Khamis, Tero Karras, and Gordon Wetzstein. 2022. Efficient Geometry-aware 3D Generative Adversarial Networks. In *CVPR*.
- Angel X Chang, Thomas Funkhouser, Leonidas Guibas, Pat Hanrahan, Qixing Huang, Zimo Li, Silvio Savarese, Manolis Savva, Shuran Song, Hao Su, et al. 2015. Shapenet: An information-rich 3d model repository. *arXiv preprint arXiv:1512.03012* (2015).
- Zhiqin Chen and Hao Zhang. 2019. Learning implicit fields for generative shape modeling. In *Proceedings of the IEEE/CVF Conference on Computer Vision and Pattern Recognition*, 5939–5948.
- An-Chieh Cheng, Xueting Li, Sifei Liu, Min Sun, and Ming-Hsuan Yang. 2022. Autoregressive 3d shape generation via canonical mapping. *arXiv preprint arXiv:2204.01955* (2022).
- Julian Chibane, Thiemo Alldieck, and Gerard Pons-Moll. 2020. Implicit functions in feature space for 3d shape reconstruction and completion. In *Proceedings of the IEEE/CVF Conference on Computer Vision and Pattern Recognition*, 6970–6981.
- Gene Chou, Yuval Bahat, and Felix Heide. 2022. DiffusionSDF: Conditional Generative Modeling of Signed Distance Functions. *arXiv preprint arXiv:2211.13757* (2022).
- Christopher Bongsoo Choy, Danfei Xu, JunYoung Gwak, Kevin Chen, and Silvio Savarese. 2016. 3D-R2N2: A Unified Approach for Single and Multi-view 3D Object Reconstruction. *European conference on computer vision* (2016), 628–644.

- Angela Dai, Christian Diller, and Matthias Nießner. 2020. Sg-nn: Sparse generative neural networks for self-supervised scene completion of rgb-d scans. In *Proceedings of the IEEE/CVF Conference on Computer Vision and Pattern Recognition*. 849–858.
- Angela Dai, Charles Ruizhongtai Qi, and Matthias Nießner. 2017. Shape completion using 3d-encoder-predictor cnns and shape synthesis. In *Proceedings of the IEEE conference on computer vision and pattern recognition*. 5868–5877.
- Jacob Devlin, Ming-Wei Chang, Kenton Lee, and Kristina Toutanova. 2018. Bert: Pre-training of deep bidirectional transformers for language understanding. *arXiv preprint arXiv:1810.04805* (2018).
- Alexey Dosovitskiy, Lucas Beyer, Alexander Kolesnikov, Dirk Weissenborn, Xiaohua Zhai, Thomas Unterthiner, Mostafa Dehghani, Matthias Minderer, Georg Heigold, Sylvain Gelly, Jakob Uszkoreit, and Neil Houlsby. 2021. An Image is Worth 16x16 Words: Transformers for Image Recognition at Scale. *ICLR* (2021).
- Philipp Erler, Paul Guerrero, Stefan Ohrhallinger, Niloy J Mitra, and Michael Wimmer. 2020. Points2surf learning implicit surfaces from point clouds. In *European Conference on Computer Vision*. Springer, 108–124.
- Patrick Esser, Robin Rombach, and Björn Ommer. 2021. Taming transformers for high-resolution image synthesis. In *Proceedings of the IEEE/CVF Conference on Computer Vision and Pattern Recognition*. 12873–12883.
- Kyle Genova, Forrester Cole, Avneesh Sud, Aaron Sarna, and Thomas Funkhouser. 2020. Local deep implicit functions for 3d shape. In *Proceedings of the IEEE/CVF Conference on Computer Vision and Pattern Recognition*. 4857–4866.
- Rohit Girdhar, David F Fouhey, Mikel Rodriguez, and Abhinav Gupta. 2016. Learning a predictable and generative vector representation for objects. In *European Conference on Computer Vision*. Springer, 484–499.
- Ian Goodfellow, Jean Pouget-Abadie, Mehdi Mirza, Bing Xu, David Warde-Farley, Sherjil Ozair, Aaron Courville, and Yoshua Bengio. 2014. Generative adversarial nets. *Advances in Neural Information Processing Systems* 27 (2014), 2672–2680.
- Meng-Hao Guo, Jun-Xiong Cai, Zheng-Ning Liu, Tai-Jiang Mu, Ralph R Martin, and Shi-Min Hu. 2021. Pct: Point cloud transformer. *Computational Visual Media* 7, 2 (2021), 187–199.
- Christian Häne, Shubham Tulsiani, and Jitendra Malik. 2017. Hierarchical surface prediction for 3d object reconstruction. In *2017 International Conference on 3D Vision (3DV)*. IEEE, 412–420.
- Kaiming He, Xiangyu Zhang, Shaoqing Ren, and Jian Sun. 2016. Deep residual learning for image recognition. In *Proceedings of the IEEE conference on computer vision and pattern recognition*. 770–778.
- Jonathan Ho, Ajay Jain, and Pieter Abbeel. 2020. Denoising diffusion probabilistic models. *Advances in Neural Information Processing Systems* 33 (2020), 6840–6851.
- Ka-Hei Hui, Ruihui Li, Jingyu Hu, and Chi-Wing Fu. 2022. Neural wavelet-domain diffusion for 3d shape generation. In *SIGGRAPH Asia 2022 Conference Papers*. 1–9.
- Moritz Ibing, Isaak Lim, and Leif Kobbelt. 2021. 3d shape generation with grid-based implicit functions. In *Proceedings of the IEEE/CVF Conference on Computer Vision and Pattern Recognition*. 13559–13568.
- Andrew Jaegle, Felix Gimeno, Andy Brock, Oriol Vinyals, Andrew Zisserman, and Joao Carreira. 2021. Perceiver: General perception with iterative attention. In *International conference on machine learning*. PMLR, 4651–4664.
- Chiyu Jiang, Avneesh Sud, Ameesh Makadia, Jingwei Huang, Matthias Nießner, Thomas Funkhouser, et al. 2020. Local implicit grid representations for 3d scenes. In *Proceedings of the IEEE/CVF Conference on Computer Vision and Pattern Recognition*. 6001–6010.
- Tero Karras, Miika Aittala, Timo Aila, and Samuli Laine. 2022. Elucidating the Design Space of Diffusion-Based Generative Models. In *Proc. NeurIPS*.
- Diederik P. Kingma and Max Welling. 2014. Auto-Encoding Variational Bayes. In *International Conference on Learning Representations (ICLR)*, Yoshua Bengio and Yann LeCun (Eds.).
- Yann LeCun, Sumit Chopra, Raia Hadsell, M Ranzato, and F Huang. 2006. A tutorial on energy-based learning. *Predicting structured data* 1, 0 (2006).
- Tianyang Li, Xin Wen, Yu-Shen Liu, Hua Su, and Zhizhong Han. 2022. Learning deep implicit functions for 3D shapes with dynamic code clouds. In *Proceedings of the IEEE/CVF Conference on Computer Vision and Pattern Recognition*. 12840–12850.
- William E Lorensen and Harvey E Cline. 1987. Marching cubes: A high resolution 3D surface construction algorithm. *ACM siggraph computer graphics* 21, 4 (1987), 163–169.
- Andreas Lugmayr, Martin Danelljan, Andrés Romero, Fisher Yu, Radu Timofte, and Luc Van Gool. 2022. RePaint: Inpainting using Denoising Diffusion Probabilistic Models. *ArXiv abs/2201.09865* (2022).
- Shitong Luo and Wei Hu. 2021. Diffusion probabilistic models for 3d point cloud generation. In *Proceedings of the IEEE/CVF Conference on Computer Vision and Pattern Recognition*. 2837–2845.
- Donald JR Meagher. 1980. *Octree encoding: A new technique for the representation, manipulation and display of arbitrary 3-d objects by computer*. Electrical and Systems Engineering Department Rensselaer Polytechnic . . . .
- Lars Mescheder, Michael Oechsle, Michael Niemeyer, Sebastian Nowozin, and Andreas Geiger. 2019. Occupancy networks: Learning 3d reconstruction in function space. In *Proceedings of the IEEE/CVF conference on computer vision and pattern recognition*. 4460–4470.
- Mateusz Michalkiewicz, Jhony K Pontes, Dominic Jack, Mahsa Baktashmotlagh, and Anders Eriksson. 2019. Deep level sets: Implicit surface representations for 3d shape inference. *arXiv preprint arXiv:1901.06802* (2019).
- Ben Mildenhall, Pratul P. Srinivasan, Matthew Tancik, Jonathan T. Barron, Ravi Ramamoorthi, and Ren Ng. 2020. NeRF: Representing Scenes as Neural Radiance Fields for View Synthesis. In *ECCV*.
- Paritosh Mittal, Yen-Chi Cheng, Maneesh Singh, and Shubham Tulsiani. 2022. Autosdf: Shape priors for 3d completion, reconstruction and generation. In *Proceedings of the IEEE/CVF Conference on Computer Vision and Pattern Recognition*. 306–315.
- Kaichun Mo, Paul Guerrero, Li Yi, Hao Su, Peter Wonka, Niloy Mitra, and Leonidas Guibas. 2019. StructureNet: Hierarchical Graph Networks for 3D Shape Generation. *ACM Transactions on Graphics (TOG), Siggraph Asia 2019* 38, 6 (2019), Article 242.
- Charlie Nash, Yaroslav Ganin, SM Ali Eslami, and Peter Battaglia. 2020. Polygen: An autoregressive generative model of 3d meshes. In *International conference on machine learning*. PMLR, 7220–7229.
- Jeong Joon Park, Peter Florence, Julian Straub, Richard Newcombe, and Steven Lovegrove. 2019. DeepSDF: Learning continuous signed distance functions for shape representation. In *Proceedings of the IEEE/CVF conference on computer vision and pattern recognition*. 165–174.
- Songyou Peng, Michael Niemeyer, Lars Mescheder, Marc Pollefeys, and Andreas Geiger. 2020. Convolutional occupancy networks. In *European Conference on Computer Vision*. Springer, 523–540.
- Ben Poole, Ajay Jain, Jonathan T Barron, and Ben Mildenhall. 2022. Dreamfusion: Text-to-3d using 2d diffusion. *arXiv preprint arXiv:2209.14988* (2022).
- Charles R Qi, Hao Su, Kaichun Mo, and Leonidas J Guibas. 2017a. Pointnet: Deep learning on point sets for 3d classification and segmentation. In *Proceedings of the IEEE conference on computer vision and pattern recognition*. 652–660.
- Charles Ruizhongtai Qi, Li Yi, Hao Su, and Leonidas J Guibas. 2017b. Pointnet++: Deep hierarchical feature learning on point sets in a metric space. *Advances in neural information processing systems* 30 (2017).
- Aditya Ramesh. 2022. Hierarchical Text-Conditional Image Generation with CLIP Latents.
- Danilo Rezende and Shakir Mohamed. 2015. Variational Inference with Normalizing Flows. In *International Conference on Machine Learning*. 1530–1538.
- Gernot Riegler, Ali Osman Ulusoy, Horst Bischof, and Andreas Geiger. 2017b. Octnetfusion: Learning deep fusion from data. In *2017 International Conference on 3D Vision (3DV)*. IEEE, 57–66.
- Gernot Riegler, Ali Osman Ulusoy, and Andreas Geiger. 2017a. Octnet: Learning deep 3d representations at high resolutions. In *Proceedings of the IEEE Conference on Computer Vision and Pattern Recognition*, Vol. 3.
- Robin Rombach, Andreas Blattmann, Dominik Lorenz, Patrick Esser, and Björn Ommer. 2022. High-resolution image synthesis with latent diffusion models. In *Proceedings of the IEEE/CVF Conference on Computer Vision and Pattern Recognition*. 10684–10695.
- Chitwan Saharia, William Chan, Saurabh Saxena, Lala Li, Jay Whang, Emily Denton, Seyed Kamyar Seyed Ghasemipour, Burcu Karagol Ayan, S Sara Mahdavi, Rapha Gontijo Lopes, et al. 2022. Photorealistic Text-to-Image Diffusion Models with Deep Language Understanding. *arXiv preprint arXiv:2205.11487* (2022).
- Mehdi SM Sajjadi, Olivier Bachem, Mario Lucic, Olivier Bousquet, and Sylvain Gelly. 2018. Assessing generative models via precision and recall. *Advances in neural information processing systems* 31 (2018).
- Mehdi SM Sajjadi, Henning Meyer, Etienne Pot, Urs Bergmann, Klaus Greff, Noha Radwan, Suhani Vora, Mario Lucic, Daniel Duckworth, Alexey Dosovitskiy, et al. 2022. Scene representation transformer: Geometry-free novel view synthesis through set-latent scene representations. In *Proceedings of the IEEE/CVF Conference on Computer Vision and Pattern Recognition*. 6229–6238.
- J Ryan Shue, Eric Ryan Chan, Ryan Po, Zachary Ankner, Jiajun Wu, and Gordon Wetzstein. 2022. 3D Neural Field Generation using Triplane Diffusion. *arXiv preprint arXiv:2211.16677* (2022).
- Yongbin Sun, Yue Wang, Ziwei Liu, Joshua Siegel, and Sanjay Sarma. 2020. Pointgrow: Autoregressively learned point cloud generation with self-attention. In *Proceedings of the IEEE/CVF Winter Conference on Applications of Computer Vision*. 61–70.
- Jiapeng Tang, Jiabao Lei, Dan Xu, Feiyang Ma, Kui Jia, and Lei Zhang. 2021. Sa-convnet: Sign-agnostic optimization of convolutional occupancy networks. In *Proceedings of the IEEE/CVF International Conference on Computer Vision*. 6504–6513.
- Maxim Tatarchenko, Alexey Dosovitskiy, and Thomas Brox. 2017. Octree Generating Networks: Efficient Convolutional Architectures for High-resolution 3D Outputs. In *2017 IEEE International Conference on Computer Vision (ICCV)*. 2107–2115.
- Aaron Van Den Oord, Oriol Vinyals, et al. 2017. Neural discrete representation learning. *Advances in neural information processing systems* 30 (2017).
- Ashish Vaswani, Noam Shazeer, Niki Parmar, Jakob Uszkoreit, Llion Jones, Aidan N Gomez, Łukasz Kaiser, and Illia Polosukhin. 2017. Attention is all you need. *Advances in neural information processing systems* 30 (2017).
- Peng-Shuai Wang, Yang Liu, Yu-Xiao Guo, Chun-Yu Sun, and Xin Tong. 2017. O-cnn: Octree-based convolutional neural networks for 3d shape analysis. *ACM Transactions on Graphics (TOG)* 36, 4 (2017), 72.

- Peng-Shuai Wang, Chun-Yu Sun, Yang Liu, and Xin Tong. 2018. Adaptive O-CNN: a patch-based deep representation of 3D shapes. In *SIGGRAPH Asia 2018 Technical Papers*. ACM, 217.
- Yue Wang, Yongbin Sun, Ziwei Liu, Sanjay E Sarma, Michael M Bronstein, and Justin M Solomon. 2019. Dynamic graph cnn for learning on point clouds. *Acm Transactions On Graphics (tog)* 38, 5 (2019), 1–12.
- Francis Williams, Zan Gojcic, Sameh Khamis, Denis Zorin, Joan Bruna, Sanja Fidler, and Or Litany. 2022. Neural fields as learnable kernels for 3d reconstruction. In *Proceedings of the IEEE/CVF Conference on Computer Vision and Pattern Recognition*. 18500–18510.
- Jiajun Wu, Chengkai Zhang, Tianfan Xue, Bill Freeman, and Josh Tenenbaum. 2016. Learning a probabilistic latent space of object shapes via 3d generative-adversarial modeling. In *Advances in Neural Information Processing Systems*. 82–90.
- Zhirong Wu, Shuran Song, Aditya Khosla, Fisher Yu, Linguang Zhang, Xiaoou Tang, and Jianxiong Xiao. 2015. 3d shapenets: A deep representation for volumetric shapes. In *Proceedings of the IEEE conference on computer vision and pattern recognition*. 1912–1920.
- Jianwen Xie, Yang Lu, Song-Chun Zhu, and Yingnian Wu. 2016. A theory of generative convnet. In *International Conference on Machine Learning*. PMLR, 2635–2644.
- Jianwen Xie, Yifei Xu, Zilong Zheng, Song-Chun Zhu, and Ying Nian Wu. 2021. Generative pointnet: Deep energy-based learning on unordered point sets for 3d generation, reconstruction and classification. In *Proceedings of the IEEE/CVF Conference on Computer Vision and Pattern Recognition*. 14976–14985.
- Jianwen Xie, Zilong Zheng, Ruiqi Gao, Wenguan Wang, Song-Chun Zhu, and Ying Nian Wu. 2020. Generative VoxelNet: learning energy-based models for 3D shape synthesis and analysis. *IEEE Transactions on Pattern Analysis and Machine Intelligence* (2020).
- Xingguang Yan, Liqiang Lin, Niloy J Mitra, Dani Lischinski, Daniel Cohen-Or, and Hui Huang. 2022. Shapeformer: Transformer-based shape completion via sparse representation. In *Proceedings of the IEEE/CVF Conference on Computer Vision and Pattern Recognition*. 6239–6249.
- Guandao Yang, Xun Huang, Zekun Hao, Ming-Yu Liu, Serge Belongie, and Bharath Hariharan. 2019. Pointflow: 3d point cloud generation with continuous normalizing flows. In *Proceedings of the IEEE/CVF International Conference on Computer Vision*. 4541–4550.
- Xiaohui Zeng, Arash Vahdat, Francis Williams, Zan Gojcic, Or Litany, Sanja Fidler, and Karsten Kreis. 2022. LION: Latent Point Diffusion Models for 3D Shape Generation. *arXiv preprint arXiv:2210.06978* (2022).
- Biao Zhang, Matthias Nießner, and Peter Wonka. 2022. 3DILG: Irregular Latent Grids for 3D Generative Modeling. In *Advances in Neural Information Processing Systems*. <https://openreview.net/forum?id=RO0wSr3R7y->
- Hengshuang Zhao, Li Jiang, Jiaya Jia, Philip HS Torr, and Vladlen Koltun. 2021. Point transformer. In *Proceedings of the IEEE/CVF International Conference on Computer Vision*. 16259–16268.
- Xin-Yang Zheng, Yang Liu, Peng-Shuai Wang, and Xin Tong. 2022. SDF-StyleGAN: Implicit SDF-Based StyleGAN for 3D Shape Generation. In *Comput. Graph. Forum (SGP)*.
- Linqi Zhou, Yilun Du, and Jiajun Wu. 2021. 3d shape generation and completion through point-voxel diffusion. In *Proceedings of the IEEE/CVF International Conference on Computer Vision*. 5826–5835.